Design and modeling of novel low-pressure nanofiltration hollow fiber modules for water softening and desalination pretreatment

Citation: Labban, Omar, et al. "Design and Modeling of Novel Low-Pressure Nanofiltration Hollow Fiber Modules for Water Softening and Desalination Pretreatment." Desalination, vol. 439, Aug. 2018, pp. 58–72.

As Published: http://dx.doi.org/10.1016/j.desal.2018.04.002

Publisher: Elsevier

Persistent URL: http://hdl.handle.net/1721.1/115392

Version: Original manuscript: author's manuscript prior to formal peer review

Design and Modeling of Novel Low-Pressure Nanofiltration Hollow Fiber Modules for Water Softening and Desalination Pretreatment

Omar Labban[a], Tzyy Haur Chong[b,c], John H. Lienhard V[a,*]

[a] *Center for Clean Water and Clean Energy, Department of Mechanical Engineering, Massachusetts Institute of Technology, Cambridge MA 02139-4307, USA*

[b] *School of Civil and Environmental Engineering, Nanyang Technological University, Singapore 639798, Singapore*

[c] *Singapore Membrane Technology Centre, Nanyang Environment and Water Research Institute, Nanyang Technological University, Singapore 637141, Singapore*

Abstract

Given its high surface area to volume ratio and desirable mass transfer characteristics, the hollow fiber module configuration has been central to the development of RO and UF technologies over the past five decades. Recent studies have demonstrated the development of a novel class of low-pressure nanofiltration (NF) hollow fiber membranes with great promise for scale-up implementation. Further progress on large-scale deployment, however, has been restrained by the lack of an accurate predictive model, to guide module design and operation. Earlier models targeting hollow fiber modules are only suitable for RO or UF. In this work, we propose a new modeling approach suitable for NF based on the implementation of mass and momentum balances, coupled with a validated membrane transport model based on the extended Nernst-Planck equation to predict module performance at the system-level. Modeling results are validated with respect to synthetic seawater experiments reported in an earlier work. A preliminary module design is proposed, and parametric studies are employed to investigate the effect of varying key system parameters and elucidate the tradeoffs available during design. The model has significant implications for low-pressure nanofiltration, as well as hollow fiber NF module design and operation.

Keywords: nanofiltration; hollow fiber module; system-level modeling; seawater pretreatment in desalination; energy consumption

O. Labban, T.H. Chong, J.H. Lienhard V, "Design and Modeling of Novel Low-Pressure Nanofiltration Hollow Fiber Modules for Water Softening and Desalination Pretreatment," *Desalination*, **439**:58-72, 1 August 2018.

*Corresponding author: lienhard@mit.edu

Nomenclature

Roman Symbols

A	Debye–Hückel constant, $m^{3/2}/mol^{1/2}$
A_c	Flow cross-sectional area, m^2
A_k	Membrane porosity
c_i	Solute concentration, mol/m^3
d_i	Fiber inner diameter, m
d_o	Fiber outer diameter, m
CP_i	Concentration polarization factor
$D_{i,p}$	Diffusion coefficient in the pore, m^2/s
$D_{i,\infty}$	Diffusion coefficient in the bulk, m^2/s
D_f	Fractal dimension
D_h	Hydraulic diameter, m
$D_{i,module}$	Module inner diameter, m
e	Specific energy consumption, kWh/m^3
e_0	Elementary charge, 1.60218×10^{-19} C
f_D	Darcy friction factor
F	Farady constant, 96485.3 C/mol
I	Ionic strength, mol/m^3
J_v	Permeate flux, $m^3/m^2 \cdot$ s
k	Boltzmann constant, 1.38065×10^{-23} J/K
$k_{c,i}$	Solute mass transfer coefficient, m/s
$K_{i,c}$	Convection hindrance factor
$K_{i,d}$	Diffusion hindrance factor
L	Module length, m
N_A	Avogadro's number, 6.02214×10^{23} mol^{-1}
N_f	Number of fibers in the module
$\dot{N}_i$	Molar flow rate of species i, mol/s
P_w	Wetted perimeter, m
Q	Volumetric flow rate, m^3/s
r_p	Effective pore radius, m
r_i	Solute Stokes radius, m
R	Universal gas constant, 8.31446 J/mol K
R_{ex}	Experimental solute rejection
R_i	Modelled solute rejection
RR	Recovery ratio

Re	Reynolds number
Sc	Schmidt number
Sh	Sherwood number
T	Temperature, K
V	Channel bulk velocity, m/s
X_d	Membrane charge density, mol/m^3
z_i	Ion valency

Greek Symbols

Δz	Cell thickness, m
ΔP	Applied pressure difference across the membrane, Pa
$\Delta\Pi$	Osmotic pressure difference across the membrane, Pa
ΔW_i	Born solvation energy barrier, J
Δx	Thickness of membrane active layer, m
γ_i	Activity coefficient
λ_i	Ratio of solute Stokes radius to effective pore radius
μ	Solvent viscosity, Pa $\cdot$ s
ϕ	Packing density
ϕ_i	Ratio of permeate flux to the uncorrected mass transfer coefficient
Φ_i	Steric partitioning coefficient
Φ_B	Born solvation coefficient
ψ	Electric potential, V
Ψ_f	Correction factor for fractal dimension
ρ	Solution density, kg/m^3
ε_0	Permittivity of vacuum, 8.85419×10^{-12} F/m
ε_b	Relative permittivity/dielectric constant of the bulk
ε_p	Relative permittivity/dielectric constant of the pore
ε_r	Relative permittivity/dielectric constant
ξ	Electric potential gradient at the feed/membrane interface, V/m
Ξ_i	Mass transfer coefficient correction factor

Subscripts

b	bulk feed solution
D	Donnan
D_h	hydraulic diameter
f	feed
in	inlet

L	hydraulic loss
p	permeate
w	condition at the wall

Superscripts

$\bullet$	Mass transfer correction for the suction effect
$*$	optimal feed flow rate for a given pressure

1. Introduction

Nanofiltration (NF), introduced in late 80's, is a membrane process whose performance falls between ultrafiltration (UF) and reverse osmosis (RO); and as its name implies, has pore sizes on the order of 1 nm (corresponding to a molecular weight cut-off, or MWCO, of $300-500$ Da) [1]. With their unique selectivities and high permeabilities relative to RO, NF membranes presented a major milestone in membrane technology, have attracted considerable attention since their introduction, and have found numerous applications, spanning numerous fields from water and waste water treatment to biotechnological, pharmaceutical, and food industry applications [2]. A recent review by Mohammad et al. [2] identifies NF as a research domain of surging interest, predicts NF will continue to play a prominent role in membrane technology, and reveals the future prospects and areas of potential growth NF is likely to experience in the long term. Recent studies have demonstrated the development of a novel class of low-pressure NF hollow fiber membranes with great promise for scale-up implementation [3, 4, 5]. The design of hollow fiber membrane modules based on those membranes is the focus of the current work.

Given its high selectivity for monovalent ions, areas in which NF is projected to grow include hard water softening, and more recently, desalination pretreatment. While traditional softening technologies, such as lime softening and pellet softening, have been challenged by their large sludge production and chemical consumption, NF has emerged as a viable alternative [6, 7]. Apart from traditional softening, NF desalination pretreatment has lately been gaining attention as evident from a recent review on integrated/hybrid membrane processes in desalination and water treatment by Ang et al. [8]. The review cites evidence that NF desalination pretreatment not only improves desalination feeds by reducing scaling, but also allows seawater reverse osmosis (SWRO) to run at lower pressures and potentially achieve higher recoveries [8]. In search of the optimal conditions for NF/SWRO desalination, Park et al. followed with their study on NF pretreatment and its effect on SWRO recovery under different conditions, and concluded that the NF/SWRO configuration featured an improvement in the quality of recovered water, especially at high recoveries [9]. More recent works from Roy et al. [10, 11] explore the effect of temperature on NF pretreatment and scale prevention in thermal desalination.

As becomes apparent from Bergman's cost analysis of softening technologies, however, one primary limitation on the economic viability of the NF pretreatment system has been the additional energy penalty incurred by the process [7]. Consequently, the requirement of lower energy consumption has occupied membrane researchers and process designers alike in search of better separation efficacy. While most NF membranes have been thin film composite (TFC) flat sheet membranes, a novel class of low-pressure NF hollow fiber membranes developed using layer-by-layer (LbL) polyelectrolyte deposition with chemical cross-linking appears to provide a solution [3, 4, 5]. According to performance tests reported in earlier work [4, 5], the newly developed membranes fared well when compared to state-of-the-art in softening and possessed superior softening performance compared to commercial NF membranes while operating at pressures that did not exceed 5 bar. These results prove the membrane's potential, raising research interest for potential large-scale

implementation.

Despite their great potential, further progress on scale-up implementation of these or other NF hollow fiber membranes is restrained by the lack of information on large-scale or commercial NF hollow fiber modules, which is necessary to evaluate a membrane's potential for scaling-up. In this work, we develop a mathematical model to our knowledge the first to predict the performance of NF hollow fiber modules on the system-level, building from experiments run on a bench-scale setup. In an earlier study, we demonstrated the successful implementation of a membrane transport model, introduced by Geraldes and Alves [12] based on the extended Nernst-Planck equation, to the newly developed LbL hollow fiber membranes [13]. However, that model focused on coupon-sized systems, and did not take into consideration the streamwise variations that will be inherent in large-scale applications. To address this need, a new model, taking a deeper look into the fundamentals governing fluid flow and mass transfer in hollow fiber modules, becomes necessary.

Since they were first patented in 1966 by DOW Chemical Company [14] followed by DuPont [15], research and development on hollow fiber membrane modules has made significant progress. These modules became attractive from an application standpoint given their desirable mass transfer characteristics and high surface area to volume ratio, which could reasonably reach 10 times that of a spiral-wound module [16]. Consequently, hollow fiber modules have found applications across a broad spectrum of fields, ranging from desalination and water treatment to gas separation, hemodialysis, blood fraction, and hydrocarbon separation [17].

The first attempts to model these systems were reported in the early 1970's with the works of Hermans [18] and Gill and Bansal [19] on RO hollow fiber modules. These authors developed their models based on first principles, namely two dimensional mass and momentum conservation equations. From there, later work focused on incorporating a diffusion transport model [20] and accounting for concentration polarization [21]. More recent works have targeted the nonuniformity and randomness that characterize hollow fiber modules [22], proposing approaches to modeling them [23, 24], such as the Voronoi tessellation method [25]. While this method presented a significant improvement, its underlying assumption of a uniform probability function for all modules makes it difficult to capture the varying degrees of packing irregularity possible under the same packing density [26]. Zhang, more recently, introduced a method based on fractal theory to approach this problem [26].

These hollow fiber modeling efforts, nonetheless, still remain unsuitable for NF, whose performance requires radically more challenging approaches. Unlike RO, NF performance is governed by the interplay of different separation mechanisms, namely sieving effects, Donnan partitioning, and dielectric exclusion. As noted by Oatley-Radcliffe et al. [27], modeling difficulty is compounded with the introduction of multi-ionic mixtures, which are of particular interest to softening and desalination applications. Following the approach first proposed by Tsuru et al. [28], the majority of NF models in literature are based on the extended Nernst-Planck equation. Having been developed for bench-scale setups, however, these models' primary limitation has been their inability to predict system-level performance or capture streamwise variations, which can be detrimental to module efficacy. In response, a previous study by Roy et al. [29] targeted the development

of comprehensive large-scale models for flat-sheet and spiral-wound NF modules, but did not consider NF hollow fiber modules.

Furthermore, the feasibility of operating at extremely low applied pressures on the large-scale is not backed by empirical evidence, and still appears questionable. Apart from the NF hollow fiber system introduced by Pentair for humic substances removal, a commercial scale NF hollow fiber module for desalination and softening applications is not currently available, nor is a well-established protocol to design these systems. The problem is further exacerbated by the lack of a practical approach to assess the viability of a specific hollow fiber membrane for such applications, and evaluate the effect different module dimensions and operating parameters can have on performance absent the need for expensive experimental procedures. These challenges combined underscore the need for further investigation in this area.

In this work, we present the development of a system-level model for NF hollow fiber modules, combining state-of-the-art NF modeling, based on the extended Nernst-Planck equation, with fundamental conservation laws that govern fluid flow and mass transfer in hollow fiber modules. The newly developed LbL1.5C membrane by Liu et al. [4] is adopted in this study, while the model presented is validated against experimental results reported in a previous work [13]. To demonstrate the model's capabilities, a preliminary module design was proposed, and parametric studies were run to assess the viability of the LbL1.5C membrane for large-scale seawater desalination pretreatment. An approach based on comparing the marginal increase in recovery to the marginal rise in applied pressure is employed to illustrate that raising applied pressure can improve energy efficiency in some conditions when operating under extremely low applied pressures, and a preliminary procedure for module sizing, inspired from the insights developed in this work, is proposed.

2. Theoretical Background

Generally, hollow fiber modules come in two primary configurations, the shell-side feed and the bore-side feed configurations [16]. In the shell-side feed systems, similar to those developed by DuPont for RO, the pressurized process stream flows on the shell-side, as the permeate seeps through the membrane and flows on the inside of the fibers. Such a setup requires the incorporation of fibers with a relatively smaller diameter to sustain the large hydrostatic pressures imposed [16]. The bore-side feed configuration, on the other hand, features a process stream flowing inside the fibers with both ends open, while the permeate flows on the shell-side, respectively. Modules of this configuration typically have fibers of larger diameters to minimize pressure drops in the feed channel [16].

This study will focus on modeling the bore-side feed configuration, shown in Fig. 1, which was also the configuration adopted by Liu et al. [3, 4]. According to Baker [16], concentration polarization is better controlled in this configuration as the occurrence of stagnant or dead zones, and feed channeling is avoided. It should be noted, nonetheless, that the small fiber diameters encountered in practice could necessitate pretreatment, depending on the feed quality, to avoid fiber clogging. Shell-side feed configurations, on the other hand, are more prone to irreversible fouling as suspended particles find themselves trapped in dead

zones [16]. Furthermore, shell-side feed configurations often suffer from significant parasitic losses in the permeate channel, which could considerably lower the driving force, and hence the permeate produced, across the module [16].

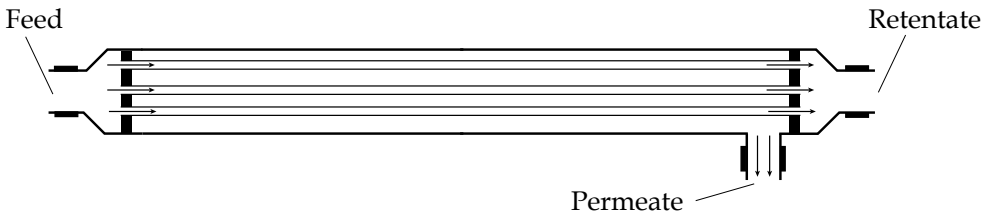

Figure 1: Schematic representation of the bore-side feed hollow fiber module configuration, featuring an inside-out filtration mode.

In this section, the developed model and its underlying assumptions are introduced and justified. Mass and momentum balances are applied, and a method to calculate the permeate flux as a function of the net driving force is proposed. The result is a system of conservation equations, while being strictly valid under the assumptions invoked, is still under-defined. As a result, we then introduce a membrane transport model to close the system and complete the analysis. Next, metrics to evaluate the module performance at the system-level are discussed. Eventually, a preliminary design for a NF hollow fiber module is proposed.

2.1. System-Level Modeling:

The first step in modeling a NF hollow fiber module involves analyzing it at the system-level through the application of mass and momentum balances. For the system at hand, feed water enters the module, where it is guided along the inside of the fibers as Fig. 1 illustrates. The result is an effective splitting of the incoming feed stream among the numerous fibers in the module. Under the assumption that all fibers are identical and independent, it follows that the process stream is divided equally among the fibers. Within each fiber, the feed stream is processed in an inside-out filtration mode, such that the permeate is collected on the module's shell-side, respectively. Once the feed water reaches the end of the module, its concentration would have already increased, leaving the system as retentate.

2.1.1. Conservation Laws:

To model the streamwise variations in the system, the fiber is divided into cells in the axial direction, as shown in Fig. 2a, and a backward first-order finite-difference scheme is implemented with a uniform grid. The boundaries of each cell form control volumes, illustrated in Fig. 2b, on which fundamental conservation laws, such as mass conservation, are applied to yield:

$$\Delta Q_f = -\Delta Q_p = -J_v\big(\pi d_i\big)\Delta z \tag{1}$$

where ΔQ_f and ΔQ_p are the finite changes in the feed and permeate volumetric flow rates across a cell, J_v is the permeate flux, d_i is the fiber inner diameter, and Δz is the step size or cell thickness.

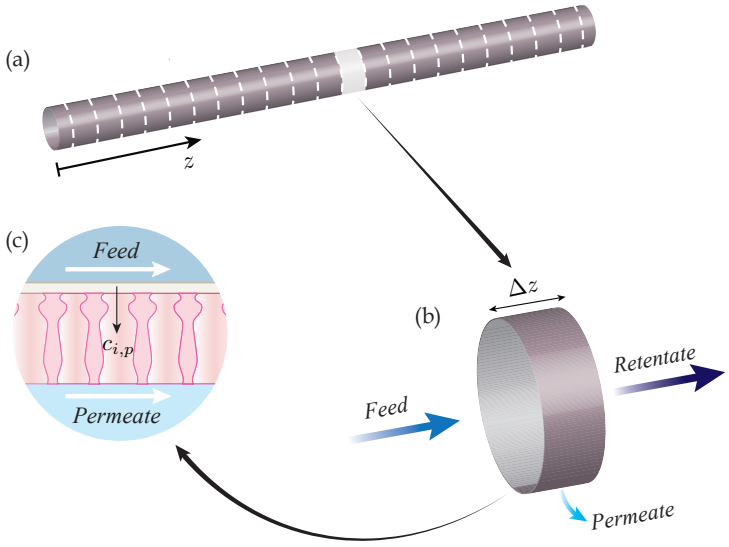

Figure 2: System-to-local level modeling: Modeling approach as applied to a single fiber to predict its separation performance. (a) The fiber is axially divided into cells; (b) conservation laws are applied across these cells; (c) a membrane transport model is coupled to the conservation laws, allowing for the permeate concentrations, $c_{i,p}$ to be determined.

Equation 1 has been derived under the assumption of constant density, such that mass conservation becomes equivalent to volume conservation. The validity of this assumption as it pertains to seawater is backed by empirical evidence showing that the density changes by less than 5% for reference salinities varying from 0 g/kg to 50 g/kg [30, 31]. The assumption is even more appropriate for NF membranes, for which the density change is expected to be lower since primarily multivalent ions are retained by the membrane. Similar to Eq. 1, conservation of species is applied to each solute in the system to arrive at:

$$\Delta \dot{N}_{i,f} = -\Delta \dot{N}_{i,p} = -J_v c_{i,p} (\pi d_i) \Delta z \tag{2}$$

where $\Delta \dot{N}_{i,f}$ and $\Delta \dot{N}_{i,p}$ are the finite changes in the feed and permeate molar flow rates of solute i aross a cell, and $c_{i,p}$ is the solute concentration in the permeate.

2.1.2. Permeate Flux and the Driving Force:

To successfully apply these equations, however, establishing the link between the permeate flux, J_v, and the net driving force across the membrane becomes necessary. This is accomplished using an empirical expression, introduced earlier by Bowen et al. [32, 33] for NF membranes, that relates the flux to the effective

driving force, $\Delta P - \Delta\Pi$, and membrane permeability:

$$J_v = \frac{r_p^2}{8\mu\Delta x_e}\big(\Delta P - \Delta\Pi\big) \tag{3}$$

where r_p is the membrane effective pore size, μ is the solution viscosity, Δx_e is the effective membrane thickness defined in line with Geraldes and Alves [12] as the ratio of membrane thickness to porosity $\Delta x/A_k$ (Section 2.2), ΔP is the applied pressure difference, and $\Delta\Pi$ is the osmotic pressure difference across the membrane. The Staverman constant is set to unity following Bowen et al. [33]. A detailed discussion of these parameters and their estimation has been covered in detail in an earlier work [13], as well as previous publications by Bowen and coworkers [32, 33, 34].

One major challenge imposed by Eq. 3 is expressing ΔP and $\Delta\Pi$ as functions of position across the module. By accounting for the hydraulic losses, the applied pressure difference can completely be expressed as:

$$\Delta P(z) = P_f(z) - P_p(z) \tag{4}$$

$$P_f(z) = P_{f,in} - \Delta P_{f,L}(z) \tag{5}$$

$$P_p(z) = P_{p,in} - \Delta P_{p,L}(z) \tag{6}$$

where $P_{f,in}$ and $P_{p,in}$ are the inlet pressures, and $\Delta P_{f,L}(z)$ $\Delta P_{p,L}(z)$ are the hydraulic losses on the feed and permeate sides, respectively.

Under steady-state operating conditions and system specifications of practical interest ($d_i/L \ll 1$ and $L/V_f \ll 1$), the flow in the fibers is expected to be laminar, and can be approximated as locally fully-developed [35]. Under this approximation, the pressure drop on the feed side can be expressed according to the Darcy–Weisbach equation [35, 36]:

$$\Delta P_{f,L}(z) = f_D \cdot \left(\frac{z}{d_i}\right) \cdot \left(\frac{\rho V_f(z)^2}{2}\right) \tag{7}$$

$$f_D = \frac{64}{\mathrm{Re}} \tag{8}$$

$$\mathrm{Re} = \frac{\rho V_f d_i}{\mu} \tag{9}$$

with f_D being the Darcy friction factor, ρ the solution density, $V_f(z)$ the feed channel bulk velocity, and Re the flow Reynolds number. The pressure drop on the shell-side, on the other hand, is more difficult to account for given the possibility of random fiber packing. According to the results reported by Zhang, who based his derivations on fractal theory, the shell-side pressure drop and the Darcy friction factor for modules with non-uniform fiber packing is evaluated according to the correlations [26]:

$$\Delta P_{p,L}(z) = f_D \cdot \left(\frac{z}{D_h}\right) \cdot \left(\frac{\rho V_p(z)^2}{2}\right) \tag{10}$$

$$f_D \mathrm{Re}_{D_h} = (-428.62\phi^3 + 620.49\phi^2 - 304.24\phi + 107.9)\Psi_f \tag{11}$$

$$\phi = N_f \left(\frac{d_i}{D_{i,module}} \right)^2 \tag{12}$$

$$\Psi_f = 1.149 D_f - 1.0 \tag{13}$$

in which $V_p(z)$ is the permeate flow velocity evaluated as the ratio of the permeate flow rate to the cross-sectional area of the permeate channel, ϕ is the packing density, D_f is the fractal dimension, and Ψ_f is a correction factor that accounts for the randomness in fiber distribution at a given packing density. According to Zhang, D_f approaches 1 for irregular packing, and 2 for regular packing; it ranges from $1.6-1.9$ for practical modules, respectively [26]. A value of $D_f = 1.7$ has been selected herein. D_h refers to the hydraulic diameter of the shell-side, and is evaluated in tandem with the definition used by Lipnizki and Field [37]:

$$D_h = \frac{4A_c}{P_w} = \frac{D_{i,module}^2 - N_f d_o^2}{D_{i,module} + N_f d_o} \tag{14}$$

with A_c being the flow cross-sectional area, P_w the wetted perimeter, $D_{i,module}$ the module inner diameter, and N_f the number of fibers in the module.

Another challenge imposed by Eq. 3 is the coupled nature of the problem. The permeate flux, as expressed in Eq. 3, is a function of the net driving pressure; and as a result, will vary with the shell-side pressure. On the other hand, the shell-side pressure is also a function of the permeate flux. A greater permeate flux will lead to larger velocities in the permeate channel, resulting in greater pressure drops on the shell-side according to the Darcy–Weisbach equation. By the same token, a greater permeate flux will lead to smaller velocities in the feed channel by conservation of mass, resulting in smaller pressure drops on the feed-side.

While it could be argued a priori that the pressure drop on the permeate side will be negligible at low permeate flow rates [29], the validity of this assumption breaks down for hollow fiber systems, operating under considerably larger packing densities or high recovery ratios. In this work, we propose an iterative approach, depicted in Fig. 3, to evaluate the pressure on the shell-side when simulating the module performance. The process starts with an initial guess of the inlet pressure on the shell-side. From there, the model is solved sequentially for the permeate flux and flow rate in each cell, allowing for an estimation of the pressure drop on the shell-side. The estimated pressure drop is then compared to the initial guess, and the process is repeated until convergence. Using this iterative approach, we later show that the shell-side pressure drop is smaller than the feed-side pressure under most operating conditions, and can reasonably be neglected, greatly simplifying the analysis.

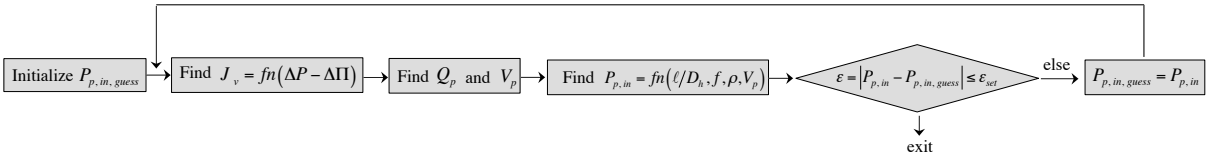

Figure 3: Algorithm employed to estimate the shell-side pressure drop.

In addition to ΔP, the osmotic pressure difference, $\Delta\Pi$, needs to be evaluated. In a work on modeling RO membranes as mass exchangers, Banchik et al. [38] demonstrated the validity of van 't Hoff's equation for salinities in the range of $0-70$ g/kg (typical of seawater desalination). The maximum deviation observed from the nonlinear osmotic pressure model was 6.8% [38]. According to this equation, the osmotic pressure may be evaluated as [39]:

$$\Delta\Pi = \Pi_f - \Pi_p = RT\left(\sum_{i=1}^{N}(c_{i,f} - c_{i,p})\right) \tag{15}$$

where the concentrations $c_{i,f}$ and $c_{i,p}$ refer to an ion's concentration in the feed and the permeate for a given salt mixture.

Since the osmotic pressure behaves as a colligative property, the equation should still hold for slight variations from seawater concentrations and compositions expected in nanofiltration. NF membranes generally, and the LbL membrane specifically, are mostly selective towards monovalent ions. Since the concentration of multivalent ions is minor in the solution, the deviation from seawater concentrations caused by their retention should also be minor, justifying the adoption of van 't Hoff's equation herein.

2.2. Local-Level Modeling: Membrane-Transport Model

While Eq. 15 completes our approach to system-level modeling, it presents yet another challenge by requiring the permeate concentration of each species, $c_{i,p}$, to be known. Since $c_{i,p}$ is a function of the membrane's selectivity, a membrane transport model is required. In this section, the choice of the transport model is addressed along with an account of the theory and its underlying assumptions.

2.2.1. Membrane-Transport Model: Model Selection

An earlier work by Oatley-Radcliffe et al. [27] highlighted state-of-the-art NF modeling as it relates to seawater desalination, and how interest has shifted from models based on irreversible thermodynamics to those based on the extended Nernst-Planck equation. Among those models, Geraldes and Alves [12] introduced *Nanofiltran*, an open-source program for modeling transport of multi-ionic solutions through NF membranes based on the extended Nernst-Planck equation. Geraldes et al. [12] validated the program against experimental results previously reported by Bowen and Mohammad [32], and analyzed its stability under a stiff NF system composed of several ions.

Several studies in the literature, such as the works of Shah et al. [40] and Deon et al. [41], have successfully implemented a similar model, noting the agreement between experiments and simulations. Furthermore, Roy

et al. successfully implemented *Nanofiltran* to predict the performance of NF flat-sheet and spiral-wound configurations at the system-level [29], and to study the effect of temperature on ion transport [10]. Similarly, Epsztein et al. [42] incorporated *Nanofiltran* in their work investigating the role of ionic charge density on Donnan exclusion. More importantly, however, the program has been demonstrated to successfully predict the performance of the novel LbL NF membranes developed by Liu et al. [5, 13], whose scaling-up is the focus of the current work. Accordingly, *Nanofiltran* is adopted herein as the transport model of choice. In the following section, the theory underlying *Nanofiltran* is briefly presented. For more details, readers are referred to the original work by Geraldes and Alves [12].

2.2.2. Nanofiltran: Theoretical background

Generally, the performance of thin film composite (TFC) membranes is primarily dictated by the membrane active layer, allowing us to neglect the membrane support layer [33]. According to the model, the flux of the i^{th} solute through the membrane active layer is governed by the extended Nernst-Planck equation with hindered transport [43]:

$$J_i = -D_{i,p}\frac{dc_i}{dx} + K_{i,c}c_i J_v - \frac{z_i c_i D_{i,p} F}{RT}\frac{d\psi}{dx} \tag{16}$$

$$D_{i,p} = K_{i,d} D_{i,\infty} \tag{17}$$

In this equation, which accounts for solute transport by diffusion, convection, and electromigration, $D_{i,p}$ is the solute diffusion coefficient in the pore, $D_{i,\infty}$ is the solute diffusion coefficient in the bulk solution, ψ is the electric potential, z_i is the ion valency, F is the Faraday constant, R is the universal gas constant, and T is the temperature. Hindered transport in the pores is accounted for through the incorporation of the hindrance factors for diffusion, $K_{i,d}$, and convection, $K_{i,c}$, expressed as a function of the ratio of solute Stokes radius to pore size, λ_i [44]. A recent work by Oatley-Radcliffe et al. [45] reviewed available correlations for the hindrance factors, and experimentally validated them for NF processes.

For $\lambda_i \leq 0.95$, the result by Dechadilok and Deen can be invoked to determine $K_{i,d}$ [44]:

$$K_{i,d} = \frac{\begin{array}{c}1.0 + (9/8)\lambda_i \ln(\lambda_i) - 1.56034\lambda_i + 0.528155\lambda_i^2 + 1.91521\lambda_i^3 \\ - 2.81903\lambda_i^4 + 0.270788\lambda_i^5 - 1.10115\lambda_i^6 - 0.435933\lambda_i^7\end{array}}{(1-\lambda_i)^2} \tag{18}$$

For $\lambda_i > 0.95$, we use the result proposed by Mavrovouniotis and Brenner [46]:

$$K_{i,d} = 0.984\left(\frac{1-\lambda_i}{\lambda_i}\right)^{5/2} \tag{19}$$

The hindrance factor for convection, $K_{i,c}$, is determined in a similar fashion using the result of Ennis et al. [47]:

$$K_{i,c} = \frac{1 + 3.867\lambda_i - 1.907\lambda_i^2 - 0.834\lambda_i^3}{1 + 1.867\lambda_i - 0.741\lambda_i^2} \tag{20}$$

Although the membranes modeled in this study are cylindrical, Cartesian coordinates can still be used in Eq. 16 with reasonable accuracy provided that $\Delta x_e/d_o \ll 1$, with Δx_e being the effective thickness of the membrane active layer and d_o the fiber outer diameter [48]. Another important constraint to satisfy inside the active layer is charge electroneutrality, taking membrane charge density X_d into consideration:

$$X_d + \sum_{i=1}^{N} z_i c_i = 0 \tag{21}$$

Apart from modeling solute transport within the membrane active layer, a model is required to describe transport across the concentration polarization layers at the membrane-feed/permeate interfaces. For membranes featuring bulk fluid flow through them, concentration polarization on the permeate side can reasonably be neglected [16]. To model concentration polarization on the feed side, however, the model developed by Geraldes and Afonso has been adopted in this study [49]. This model, which expresses the flux of the i^{th} solute through the concentration polarization layer as the sum of the fluxes due to back diffusion, convection, and electromigration as shown in Eq. 22, accounts for concentration polarization through the incorporation of a mass transfer coefficient as follows:

$$J_i = -k^{\bullet}_{c,i}(c_{i,w} - c_{i,b}) + J_v c_{i,w} - z_i c_{i,w} D_{i,\infty} \frac{F}{RT} \xi \tag{22}$$

$$k^{\bullet}_{c,i} = k_{c,i} \Xi \tag{23}$$

$$\Xi = \phi_i + (1 + 0.26\phi_i^{1.4})^{-1.7} \tag{24}$$

In Eq. 22, $c_{i,w}$ is the solute concentration at the membrane-feed interface just outside the pores, $c_{i,b}$ is the solute bulk concentration, and ξ is the electric potential gradient at the feed-membrane interface. More importantly, $k^{\bullet}_{c,i}$ refers to the mass transfer coefficient, estimated based on conventional Sherwood number correlations and corrected for the "suction effect" resulting from the permeation at the membrane interface. This correction is achieved through the incorporation of a flux-dependent correction factor, Ξ, defined in Eq. 24 with $\phi_i = J_v/k_{c,i}$ [49]. To calculate the mass transfer coefficient, $k_{c,i}$, a Sherwood number correlation, inferred for the flow inside hollow fiber membrane modules and the test conditions of interest, has been adopted [23]:

$$\mathrm{Sh}_i = 1.62\mathrm{Gz}_i^{1/3} = 1.62\mathrm{Re}^{1/3}\mathrm{Sc}_i^{1/3}(d_i/L)^{1/3}, \qquad (\mathrm{Gz}_i > 4) \tag{25}$$

$$\mathrm{Sh}_i = \frac{k_{c,i} d_i}{D_{i,\infty}} \tag{26}$$

$$\mathrm{Sc}_i = \frac{\mu}{\rho D_{i,\infty}} \tag{27}$$

where Gz_i is the solute Graetz number, Sh_i is the solute Sherwood number, Re is the flow Reynolds number, Sc_i is the solute Schmidt number, and L is the module length, respectively.

In addition to Eq. 22, another equation, Eq. 28, relating the flux of the i^{th} solute to its concentration in the permeate can be obtained from the solute continuity equation under steady state operating conditions. Two more electroneutrality conditions, expressed as Eqs. 29 and 30, should also be satisfied on the membrane-feed/permeate interfaces, respectively [12].

$$J_i = J_v c_{i,p} \tag{28}$$

$$\sum_{i=1}^{N} z_i c_{i,w} = 0 \tag{29}$$

$$\sum_{i=1}^{N} z_i c_{i,p} = 0 \tag{30}$$

Once solute transport in the active layer and the concentration polarization layer has been considered, the final step in setting up the membrane transport model is accounting for solute partitioning at the membrane-feed/permeate interfaces at chemical equilibrium. The result is two equations that act as "boundary conditions" on the membrane-feed and membrane-permeate interfaces, and are expressed as Eqs. 31 and 32 [12]:

$$\frac{\gamma_{i,1} c_{i,1}}{(\gamma_{i,w} c_{i,w})} = \Phi_i \Phi_B \exp\left(- \frac{z_i F}{RT} \psi_{D,w} \right) \tag{31}$$

$$\frac{\gamma_{i,N} c_{i,N}}{(\gamma_{i,p} c_{i,p})} = \Phi_i \Phi_B \exp\left(- \frac{z_i F}{RT} \psi_{D,p} \right) \tag{32}$$

In Eqs. 31 and 32, ψ_D refers to the Donnan potential forming across the membrane at equilibrium [50, 51], $c_{i,1}$ and $c_{i,N}$ are the concentrations just inside the pores at the feed and permeate interfaces [13], while γ_i refers to the solute activity coefficient, calculated in *Nanofiltran* based on the Davies model, which relates γ_i to the solution ionic strength, I, according to [52, 53]:

$$\ln(\gamma_i) = -A z_i^2 \left(\frac{\sqrt{I}}{1 + \sqrt{I}} - bI \right) \tag{33}$$

$$I = \frac{1}{2} \sum_{i=1}^{N} z_i^2 c_i \tag{34}$$

with b assigned a value of 0.3, and A being the temperature-dependent Debye–Hückel constant evaluated according to [53, 54]:

$$A = \left(\frac{\sqrt{2\pi N_A}}{\ln(10)} \right) \left(\frac{e_0^2}{4\pi \varepsilon_0 \varepsilon_r kT} \right)^{3/2} \tag{35}$$

where N_A is Avogadro's number, e_0 is the elementary charge, ε_0 is the vacuum permittivity, and k is the Boltzmann constant.

We note that an assumption concerning the validity of the Debye–Hückel theory inside a nanopore is being made herein. The Debye–Hückel theory assumes a bulk solution with the number of anions and cations being equal, which may be challenged inside a pore of nanometer dimension [33, 55]. Another alternative

proposed by Bowen and Welfoot [33] is to assume ideal solution behavior with activity coefficients set to unity. Given the focus of this work on large-scale modeling, however, we choose to retain the assumptions laid previously by Geraldes and Alves [12] for consistency.

Furthermore, the term Φ_i in Eqs. 31 and 32 refers to the steric partitioning coefficient that accounts for the sieving effects that result from the finite size of the solute relative to the pore [34]. On the other hand, the term Φ_B refers to the Born solvation coefficient that accounts for the solute partitioning that results from dielectric exclusion, and its associated barrier to ion solvation arising from the difference in dielectric constant between the membrane pores and the bulk solution [56, 57]. These two terms are evaluated according to Eqs. 36 and 37 [12]:

$$\Phi_i = (1 - \lambda_i)^2 \tag{36}$$

$$\Phi_B = \exp\left(-\frac{\Delta W_i}{kT}\right) \tag{37}$$

$$\Delta W_i = \frac{z_i^2 e_0^2}{8\pi\varepsilon_0 r_i}\left(\frac{1}{\varepsilon_p} - \frac{1}{\varepsilon_b}\right) \tag{38}$$

where ΔW_i is the solvation energy barrier computed based on Born's model [58], r_i is the solute's Stokes radius, and ε_b is the dielectric constant of the bulk solution.

Together, Eqs. 31 and 32 account for solute partitioning occurring as a result of steric hindrance, dielectric exclusion, and Donnan partitioning, and completely define the problem of modeling solute transport. The next steps involve discretizing the membrane's active layer, applying one extended Nernst-Planck equation for every solute at every discretization point, coupling these equations with the concentration polarization equation and boundary conditions, and finally solving the resulting system of equations numerically [13, 12]. The outcome of this computation will include the unknown permeate concentrations, $c_{i,p}$, closing the system of equations as Fig. 2c illustrates.

2.3. System-to-Local Level Modeling

Figure 2 summarizes the modeling approach presented in this work, and illustrates how the membrane transport model is coupled to the system-level analysis to provide a comprehensive model that can accurately predict the performance of a NF hollow fiber module under different operating conditions. The figure also reveals the necessary implementation of a two-dimensional discretization scheme (parallel + perpendicular to the fiber axial direction) for every solute, resulting in a three-dimensional matrix of unknowns, to solve the problem. The solver in this work was implemented using MATLAB.

The integration of a membrane transport model over the hollow fiber module not only completes the development of a model that can predict streamwise variations in system performance, but also opens the doors for design and optimization studies, and reduces the number of experiments necessary to predict system-level performance. Given the complexity and difficulty associated with predicting NF separation, such a model is essential to: (1) evaluate the performance of the hollow fiber configuration as applied

recently to NF, (2) guide the scale-up implementation of the novel low-pressure NF membranes developed, such as the LbL1.5C membrane, and (3) assess the compatibility of a specific NF membrane with desalination pretreatment applications, absent the need for expensive large-scale experiments as we show later.

2.4. Assessing Module Performance: Introducing Performance Metrics

In this section, we define the performance metrics used in this study. These metrics allow us to probe and quantify the effects different design parameters, and operating conditions could have on the system. Defined in Eq. 39, the membrane rejection ratio, R_i, measures the fraction of a solute that permeates through the membrane. The membrane rejection is a quantitative metric of the membrane's selectivity, and the quality of permeate produced. The system recovery ratio, RR, as defined in Eq. 40, measures the fraction of the permeate recovered from the process stream. For a given net driving pressure, a higher recovery ratio implies a higher membrane permeability and a greater system yield. The concentration polarization factor, CP_i, provides a measure of the significance of concentration polarization under given operating conditions, and is defined in Eq. 41. Most importantly, the specific energy consumption, e, provides a metric to evaluate the energy cost of permeate production in the module, and is defined as in Eq 42.

$$R_i = 1 - \frac{c_{i,p}}{c_{i,b}} \tag{39}$$

$$RR = \frac{Q_{p,out}}{Q_{f,in}} \tag{40}$$

$$CP_i = \frac{c_{i,w}}{c_{i,b}} \tag{41}$$

$$e = \frac{Q_{f,in}P_{f,in}}{Q_{p,out}} = \frac{P_{f,in}}{RR} \tag{42}$$

2.5. Proposed Hollow Fiber Module Configuration: Module Sizing and Design

To proceed with system-level evaluation of module performance, a reference large-scale system needs to be adopted. Driven by the lack of commercial NF hollow fiber modules for softening and desalination pretreatment applications, we propose in this section a preliminary design inspired by earlier efforts on designing UF hollow fiber modules [59]. In spite of expected similarities, NF membranes are expected to depart from UF standards when it comes to the operating conditions, namely the applied pressure and feed flow rate. Since NF membranes have tighter pore sizes relative to UF, the applied pressures are expected to be higher in NF. Driven by differences in the process streams UF and NF are designed to handle, UF hollow fibers will tend to have higher feed flow rates relative to NF to prevent membrane pore clogging. The specifications of the proposed design are summarized in Table 1.

Table 1: Nominal specifications of modeled large-scale hollow fiber module.

Specification	Nominal Value
Membrane Area	50 m^2
Module Length (L)	1.5 m
Module Diameter ($D_{i,module}$)	165 mm
Packing Density (ϕ)	75%
Fiber Inner Diameter (d_i)	1 mm
Fiber Outer Diameter (d_o)	1.38 mm
Inlet Flow Rate (Q)	1000 L/h

Similar to commercial UF hollow fiber modules, such as those developed by Dow [60] and Koch Membrane Systems [61], a total membrane area of 50 m^2 with a module length of 1.5 m, and a module diameter of 165 mm were selected. The fiber dimensions and operating pressures of the system have been set to match those of the LbL1.5C membranes as reported by Liu et al. [4]. These specifications in turn set the module's packing density at 75%. Unless otherwise specified, the inlet flow rate has been fixed at $Q = 1000$ L/h to minimize the energy consumption of the system while maintaining reasonable rejections as our results will demonstrate later.

Given the scope of our work, the model feed was chosen to be synthetic seawater, whose ion composition and properties are provided in Table 2 for reference. Since the module performance is membrane specific, and the membrane properties are also a function of the feed chemistry, we summarize in Table 3 the relevant membrane parameters characterized under these feed conditions. Details concerning the membrane characterization process are provided in the Appendix for completeness.

Table 2: Synthetic seawater composition and charged solute properties (pH = 6.5).

	Na^+	Ca^{+2}	Mg^{+2}	SO_4^{2-}	Cl^-
Ion Concentration (mg/kg)	11122	382	1394	2136	20300
r_i (nm)	0.184	0.309	0.347	0.230	0.121
D_∞ ($m^2/s \times 10^{-9}$)	1.33	0.792	0.706	1.06	2.03

Table 3: LbL1.5C DSPM-DE model parameters [13].

Parameter	r_p (nm)	Δx_e (μm)	ε_p	X_d (mol/m^3)
	0.5	1.33	41.3	-27

3. Results and Discussion

In this section, the developed model for predicting the performance of NF hollow fiber modules is validated. Parametric studies are run to investigate the effect of different parameters on module performance, and offer insights into module design. Specifically, the significance of module pressure drop, including bore-side and shell-side components, is assessed. The effect of feed flow rate on module performance is studied, and an optimal flow rate is observed. The importance of the developed model is underscored by the intensity of streamwise variations observed. Concentration polarization is examined under varying operating conditions.

More importantly, increasing module length to increase recovery will be shown to be less effective given a decaying driving force, and leading to a tradeoff between CAPEX and OPEX. A comparison of marginal increases in pressure to marginal increases in recovery is employed to show that raising pressure can reduce the specific energy consumption should the growth of RR outpace that of ΔP, respectively. This section is concluded with a simple design methodology to guide designers interested in extending the well-established hollow fiber configuration to nanofiltration.

3.1. Model Validation

To assess its accuracy, the proposed hollow fiber model was validated with respect to experimental results reported in an earlier work [13] for the LbL1.5C hollow fiber membrane developed by Liu et al. [4]. System dimensions and specifications were scaled down to match those of the experimental setup, and synthetic seawater experiments (for a feed composition matching that of Table 2 and a cross-flow velocity of 0.3 m/s) were adopted as the validation benchmark [13]. The membrane model parameters corresponding to those experiments match those reported in Table 3.

Simulation results, which were grid independent beyond 100 cells, are summarized in Table 4. Modeling results were found to agree with experimental observations, and to fall within the experimental error margins (observed deviation was within 10% for multivalent ions) [13]. In addition to experimental error, other sources of computational error responsible for the observed deviation may be attributed to the assumptions made, such as assuming a uniform distribution of fiber dimensions, an equal splitting of the feed among the individual fibers, or independence of the fibers from one another. Negative rejection, a phenomenon well reported in literature [43, 62, 63, 64] that refers to an increase in the permeate concentration relative to the feed [13], is also well predicted by the present model.

Table 4: Model validation with synthetic seawater (cross-flow velocity was maintained at 0.3 m/s) [13].

	Ca^{+2} (%)		Mg^{+2} (%)		SO_4^{2-} (%)	
	R_{ex}	R_i	R_{ex}	R_i	R_{ex}	R_i
3 bar	71.1	75.7	90.6	85.4	85.4	87.4
4 bar	78.9	84.6	93.6	91.0	86.8	92.7

3.2. Module Pressure Drop

As part of their work investigating the effect of shell-side hydrodynamics on module performance, Costello et al. [65] divided the shell-side pressure drop into a laminar component, which accounts for viscous drag along the fibers, and a turbulent component, which accounts for inertial drag due to stream splitting, channeling, and mixing. Their results reveal a trend from "inertial-drag-dominated" to "viscous-drag-dominated" pressure drop with increasing packing density. The authors attribute this shift to the non-uniformity in fiber packing, suggesting that uniform packing is more likely at higher packing densities. They concluded that these results fall in line with the view that flow on the shell-side is three-dimensional, featuring bulk flow axially and transverse flow across the fibers due to channeling [65].

To assess the impact the permeate side pressure drop has on module performance in this case, a parametric study, looking into the module hydraulic losses as a function of the packing density and applied pressure, was run. The results of this study are depicted in Fig. 4, showing the permeate-side and feed-side pressure drops as functions of packing density and applied pressure, respectively.

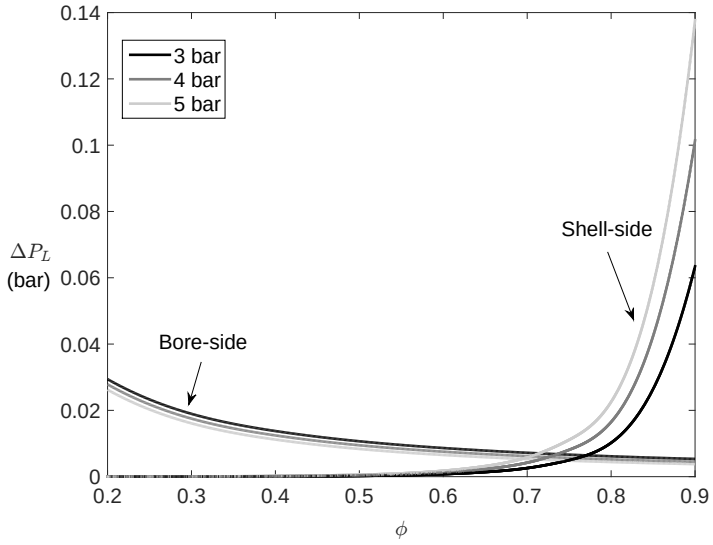

Figure 4: Bore-side (feed) and shell-side (permeate) hydraulic losses as a function of module packing density and applied pressure. Except for ϕ and its corresponding RR, all nominal specifications were fixed at the values reported in Table 1.

As the results show, the hydraulic losses in the feed channel decrease as the packing density increases since the feed flow rate, Q, is now being divided among more fibers, leading to lower velocities in each fiber. In contrast, the hydraulic losses on the shell-side increases with increasing packing density as the recovery ratio increases and hydraulic diameter gets smaller. This increasing shell-side pressure drop is similar in behavior to earlier results reported by Costello et al. [65]. Raising pressure has a similar effect by increasing the recovery ratio, which leads to higher hydraulic losses on the shell-side, and lower hydraulic losses on the feed-side. Figure 4 shows that these competing trends reach an optimum at around a packing density of 75%.

Comparing the hydraulic losses to the applied pressure applied reveals that the hydraulic losses are always a small fraction in this case. Figure 4 captures the fact that for reasonable packing densities ($\phi \leqslant 0.75$), the permeate-side pressure can be taken to be atmospheric given the low permeate velocities. Subsequently, we adopt this assumption in the model, considerably lowering its computational expense.

3.3. Optimal Flow Rate

Solute rejection is the parameter of primary interest from a softening or pretreatment perspective as it quantifies the quality of water recovered from an initial feed stream. At low feed flow rates, the feed concentration rises quickly, resulting in an increase in the osmotic pressure, and a corresponding decrease in permeate flux. Consequently, diffusion of solute species from the feed to the permeate becomes more dominant, and the permeate solution increases in concentration, ultimately reducing rejections.

To counteract this effect, which is primarily a manifestation of concentration polarization, feed flow rates need to be increased to raise mass transfer coefficients, and alleviate the rise in solute concentration along the module length. As a result, diffusive transport of species from feed to permeate is less encouraged, keeping the permeate concentration at a minimum, and ultimately increasing rejections.

To quantitatively capture this effect, Fig. 5 plots the observed rejection predicted as a function of the feed flow rate at an applied pressure of 5 bar. As the plot illustrates, the rejection increases with increasing flow rate, until a certain threshold, Q^*, is reached. Q^* is defined such that its corresponding rejection ratio is within 97% of the maximum obtainable at a flow rate of 1500 L/h. Increasing the feed flow rate beyond Q^* does not increase rejection significantly, but the energy penalty incurred from the increased pumping power continues to rise. To minimize the energy requirements associated with softening or pretreatment, while maintaining high permeate quality, Q^* represents the optimal flow rate at which the system should be run for a given operating pressure. Similar trends were observed for lower operating pressures. Since the LBL1.5C membrane selectively allows monovalent ions to permeate through as reported by Liu et al. [4], their rejection is not sensitive to changes in feed flow rates as Fig. 5 demonstrates.

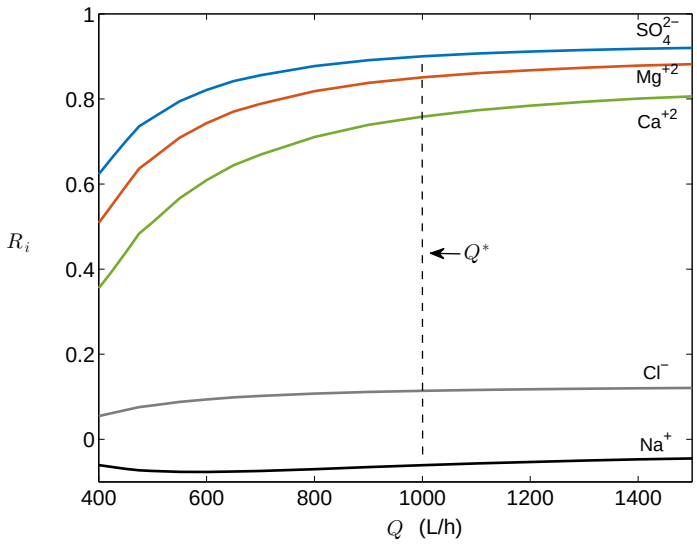

Figure 5: Module average rejection as a function of feed flow rate at an applied pressure of 5 bar. Except for Q and its corresponding RR, all nominal specifications were fixed at the values reported in Table 1.

3.4. Streamwise Variations

Another important aspect of system design is streamwise variations, which are not uncommon given the scale at which these membrane systems are implemented in practice. As the feed stream is processed along the module length, the bulk concentration of retained species in the feed channel rises. The resulting rise in feed osmotic pressure, coupled with the hydraulic losses incurred by the module, lead to decreasing rejections in the flow direction. A well-designed module should in practice be "balanced", meaning that streamwise variations from inlet to outlet are minimized, and the slopes at which the performance metrics vary per module are not steep. A well-balanced module has a relatively uniform flux, decreases the likelihood of fouling, suffers less from thermodynamic irreversibilities, and ensures the membrane area is utilized efficiently.

A parametric study was run by varying the pressure and correspoding recovery ratio, while fixing all other module specifications per the values reported in Table 1. The results are shown in Figs. 6 and 7. Figure 6 plots the streamwise variations in feed bulk concentration as a function of length across the system. As the figure illustrates, streamwise variations become more significant with increasing applied pressures, or equivalently increasing recovery ratios.

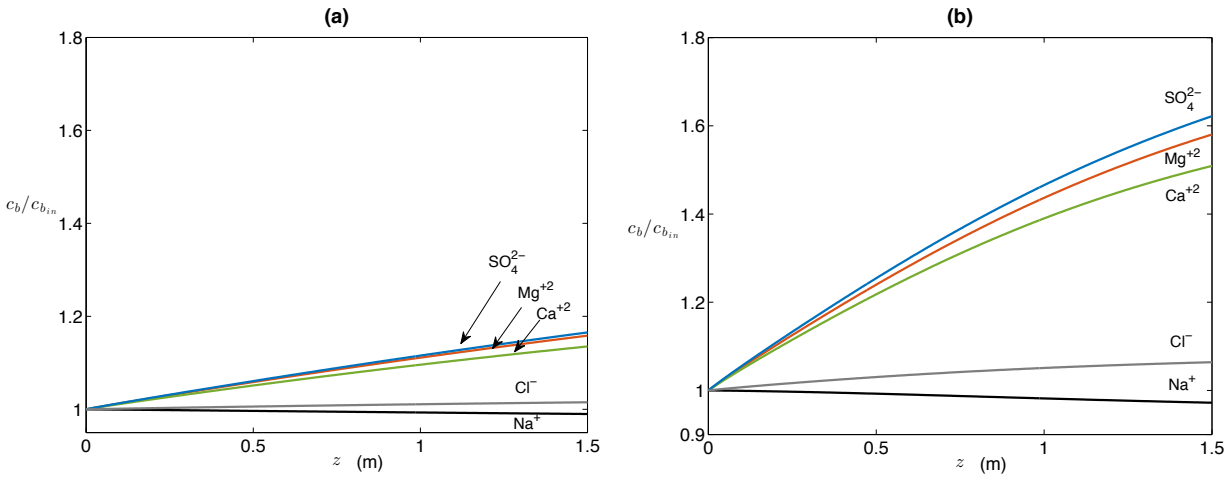

Figure 6: Streamwise variations in the feed bulk concentration: (a) applied pressure of 3 bar; (b) applied pressure of 5 bar. Except for ΔP and its corresponding RR, all nominal specifications were fixed at the values reported in Table 1.

Another point to elucidate is the order by which the concentration of the different ion species appears to be rising in the system. The trends observed are primarily a function of the selectivity of the LbL1.5C membrane as we analyzed in a previous study [13]. Since the membrane selectively passes monovalent ions, the concentrations of these ions appear to remain constant throughout the system. According to our previous results, the LbL1.5C membrane, confronted with artificial seawater, was less selective towards SO_4^{2-} given its negative charge under these operating conditions. Given its larger Stokes radius and lower diffusivity, Mg^{+2} experiences a higher rejection compared to Ca^{+2} [13]. As expected, the concentrations of SO_4^{2-} and Mg^{+2} rise the most according to Fig. 6.

As with the feed bulk concentration, ion rejection is also a function of streamwise position. As shown in Fig. 7, the membrane retention of multivalent ions drops in the streamwise direction as a result of increasing ion diffusion across the membrane, and decreasing permeate flux. The membrane rejection of monovalent ions stays relatively constant given the membrane's low rejection towards them. On the other hand, rejection drops for all multivalent ions, decreasing the most for Ca^{+2} since the membrane is more selective towards it relative to the other multivalent ions present in the solution. Similar to Fig. 6, the decrease in multivalent ion rejection becomes more significant at higher applied pressures, indicating that a rising bulk concentration, coupled with more prominent concentration polarization, acts to encourage ion transport across the membrane.

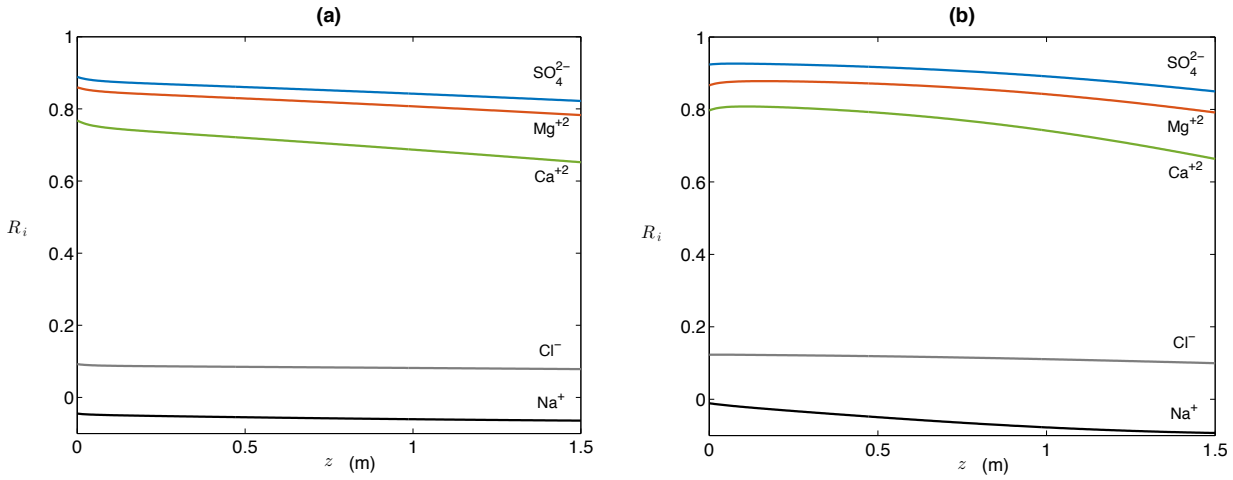

Figure 7: Streamwise variations in module rejection: (a) applied pressure of 3 bar; (b) applied pressure of 5 bar. Except for ΔP and its corresponding RR, all nominal specifications were fixed at the values reported in Table 1.

The results discussed in this section underscore the importance of streamwise variations along the module, and their impact on overall performance. Another implication of the results presented is the apparent tradeoff a designer would face between module recovery ratio, RR, and rejection, R_i. While an improved system recovery is often desirable, a compromise might be necessary to ensure that an acceptable permeate quality is maintained. In light of this discussion, concentration polarization emerges as an important variable in module design.

3.5. Concentration Polarization

Concentration polarization refers to the formation of concentration gradients at the membrane interface. From a design standpoint, concentration polarization is generally undesirable as it reduces permeate fluxes, and affects ion retentions. In this section, we investigate the magnitude of concentration polarization the proposed design is likely to experience during operation. The concentration polarization factor, CP_i, will be the primary metric used in this analysis. The results of this analysis are represented in Fig. 8.

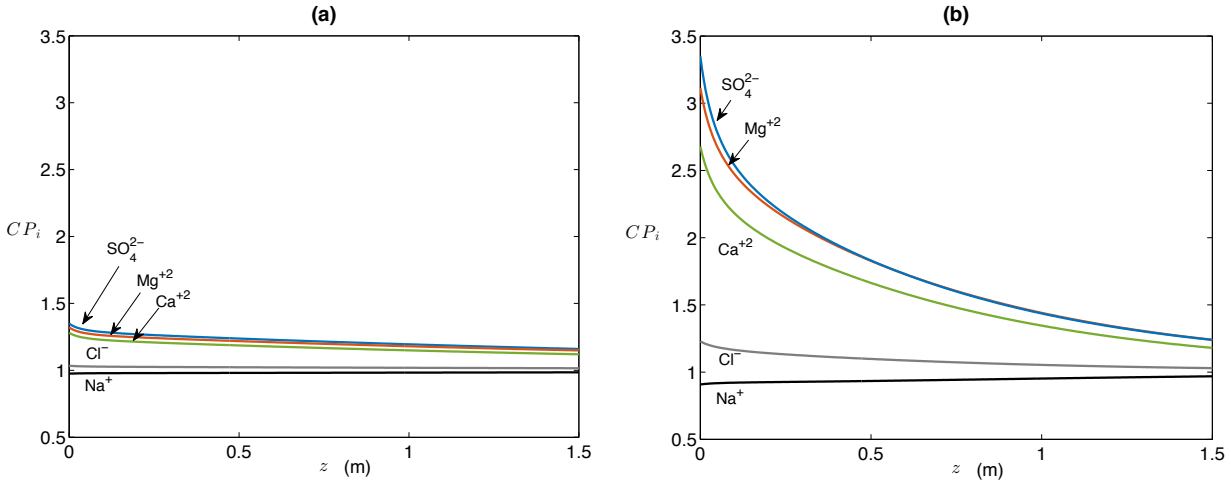

Figure 8: Streamwise variations in concentration polarization factor, CP_i: (a) applied pressure of 3 bar; (b) applied pressure of 5 bar. Except for ΔP and its corresponding RR, all nominal specifications were fixed at the values reported in Table 1.

Figure 8 depicts the streamwise variation in the concentration polarization factor across the system. Similar to Fig. 6, the order followed by the different ion species in the solution is primary a manifestation of the membrane's selectivity. The monovalent ions, which are not retained by the membrane, appear to experience very little concentration polarization. In contrast, the multivalent ions SO_4^{2-} and Mg^{+2}, which are retained the most by the membrane, appear to experience the highest concentration polarization, followed by Ca^{+2}, as evident from the concentration polarization factor.

Another observation to point out is the growing role concentration polarization plays in the system as the applied pressure increases. Interestingly, the concentration polarization factor for all retained species decreases across the length of the module. The decrease in the concentration polarization factor is primarily a result of the driving force, which diminishes across the module length as the osmotic pressure rises and the hydraulic losses accumulate. The result is a diminishing difference between the bulk and membrane concentration.

3.6. Effect of Module Length

For a fixed inlet feed flow rate, Q, two approaches are available to the designer to reach a specific recovery ratio, increasing the applied pressure or available membrane area in the system. In this section, we investigate both options by varying the applied pressure and module length, or equivalently, the number of modules connected in series. The primary limitation on increasing membrane area is the declining driving force, $\Delta P - \Delta\Pi$, along the flow direction, which renders any increase in membrane area less effective at permeate recovery. In this study, the module length and applied pressure were varied for a fixed feed flow rate, and the resulting trends are reported in Fig. 9.

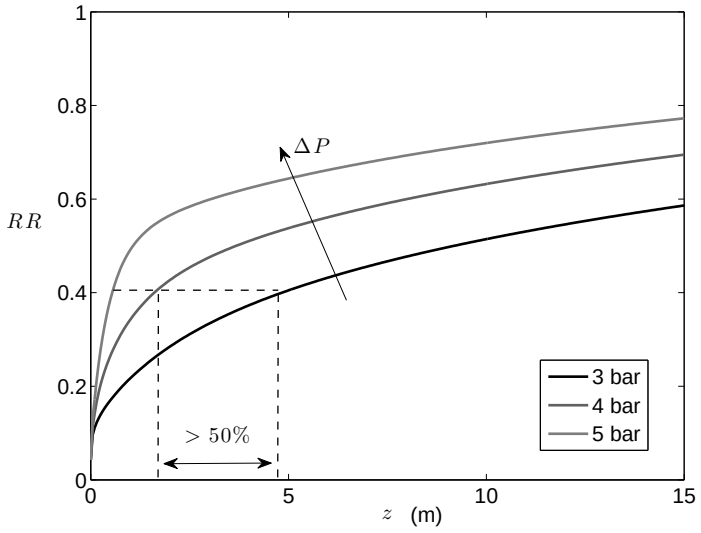

Figure 9: Effect of increasing module length and applied pressure on RR. Except for the module length, all nominal specifications were fixed at the values reported in Table 1.

According to Fig. 9, the recovery ratio increases with increasing applied pressure and membrane area as expected. One important takeaway from this figure, however, is that the system length and its corresponding recovery ratio are nonlinearly related. Stated differently, doubling the number of modules present in the system does not double the resulting recovery ratios due to the drop in driving force or flux along the length.

These results imply that while it might appear attractive to operate at lower pressures to lower the system's operational expenditure (OPEX), the additional capital expenditure (CAPEX) and OPEX from maintenance incurred by increasing the number of modules necessary to reach a specific recovery might be unjustified. For a fixed recovery ratio of 40%, for instance, our results demonstrate that raising pressure from 3 to 4 bar decreases the length required by more than a factor of two as shown in Fig. 9. Consequently, a designer should take these considerations into account when searching for an optimal operating point for the system. In the next section, we present one approach to arrive at this optimal operating point by minimizing the specific energy consumed by the system.

3.7. Module Energy Consumption

Among all metrics considered in the study, energy consumption is perhaps of primary interest as it provides a handle on the energy penalty and carbon footprint associated with the NF process. In this section, the specific energy consumption, e, is chosen as the metric to evaluate the energy consumption of the proposed design. A set of parametric studies, whose results are summarized in Figs. 10 and 11, were run to investigate the dependence of the specific energy consumption on the applied pressure and feed flow rate.

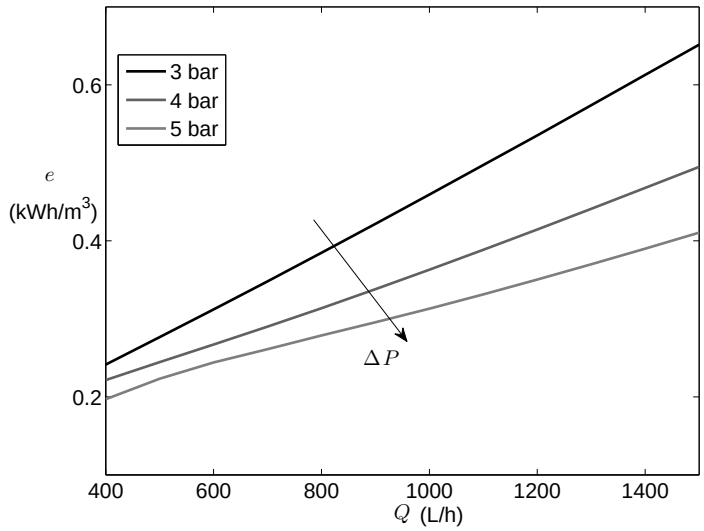

Figure 10: Specific energy consumption, e, as a function of inlet feed flow rate and applied pressure. Except for Q, all nominal specifications were fixed at the values reported in Table 1.

Figure 10 depicts the specific energy consumption of the system as a function of the inlet feed flow rate and applied pressure. The results clearly indicate an increase in the specific energy consumption with increasing feed flow rate as more pumping work becomes necessary to drive the separation process. More surprisingly, however, these results suggest that the specific energy consumption decreases with increasing applied pressure for all feed flow rates considered.

Another significant observation is that the incremental decrease in e diminishes with increasing applied pressures. Based on its definition, e could decrease with increasing applied pressures only if the recovery ratio, RR, is growing at a much faster rate relative to the applied pressure.

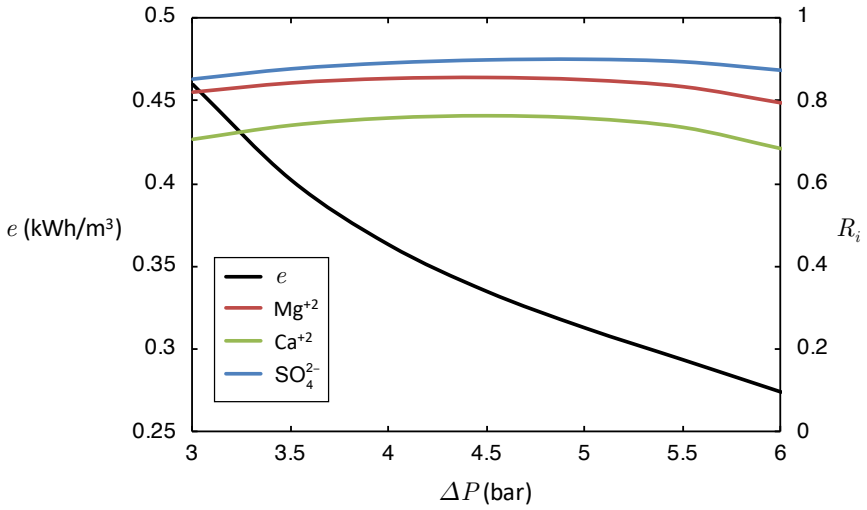

Figure 11: Specific energy consumption, e, and rejection, R_i, as a function of applied pressure, at the optimal feed flow rate of 1000 L/h.

Further analysis at the optimal feed flow rate, Q^*, reveals that the specific energy consumption decreases with increasing applied pressure as shown in Fig. 11. In accordance with the results presented in Section 3.3, the rejections of the multivalent ions at Q^* appear to be constant, nonetheless, indicating that increasing the module recovery ratios by raising the pressure does not impact the permeate quality under these conditions. These results explain the trends observed earlier in Fig. 10, and indicate that the system benefits from raising the pressure since the marginal increase in permeate produced surpasses the marginal increase in applied pressure. Recently, similar trends of decreasing e with increasing RR in seawater NF have also been observed empirically by Park and coworkers [9].

These results clearly indicate that operating at lower pressures, while it may appear attractive, could be more expensive. The insights presented in this section underscore the importance of running an analysis similar to this work's to evaluate the feasibility of a given membrane for system-level implementation in a specific application, or to help the designer locate an optimal point for operating the system.

We end this section by proposing a preliminary approach to designing a large-scale NF hollow fiber system for a given membrane, based on experiments run on a bench-scale setup. (1) A membrane needs to be characterized according to a specific membrane transport model. (2) From there, the membrane should be modeled at the system-level in an analysis similar to the one developed in this work to locate an optimal feed flow rate. (3) Once an optimal feed flow rate is established, a set of parametric studies can be executed in search of an optimal operating point, at which the specific energy consumption is minimized. (4) Eventually, this proposed design can further be refined by running experiments, coupled with sensitivity analysis and optimization studies with the presented model.

4. Conclusions

In this study, a new system-level model for NF hollow fiber membrane modules was developed following an interdisciplinary approach featuring mass and momentum balances, coupled with a transport model based on the extended Nernst-Planck equation. The overarching objective has been to present a model that empowers researchers and designers with: (1) an understanding of the physics that govern mass and momentum transport in the module, as well as the various tradeoffs that exist among design parameters and operating conditions; (2) a tool that predicts NF module performance under different operating conditions and complex feed chemistries, and enables membrane assessment for a given application, absent the need for costly large-scale experiments; and (3) criteria for module performance assessment along with a preliminary procedure for module sizing.

The LbL1.5C membrane, newly developed by Liu et al. [4], was adopted in this study, and the proposed model was validated against experimental results reported previously [13]. A preliminary bore-side feed module design was proposed, and parametric studies were run to study the effect of different parameters on module performance. Specifically, the change in hydraulic losses on the bore and shell-side of the module with packing density and applied pressure was investigated, as well as the change in module average rejection as a function of feed flow rate. Streamwise variations in feed bulk concentration and rejection were observed, and the occurrence of concentration polarization was assessed. The tradeoffs between module rejection, recovery ratio, module flow rate, length, applied pressure, and specific energy consumption have been studied.
The key findings from this study include:

1. Hydraulic losses increased on the shell-side and decreased on the bore-side, as the recovery ratio was increased, and a crossover point was observed.
2. The magnitude of the hydraulic losses on the shell-side (permeate-side) was shown to be negligible relative to the applied pressure at low to moderate packing densities.
3. Module average rejection increased with increasing inlet feed flow rate as solute transport across the membrane decreased. The decrease in solute transport is a result of the diminished occurence of concentration polarization, and the more spatially-uniform feed concentrations. The trends break down beyond a certain threshold, and an optimal feed flow rate was observed.
4. Streamwise variations in the feed bulk concentrations and rejection ratios were more prominent at higher applied pressures; and the relative magnitude of these variations was shown to be a manifestation of the membrane selectivity towards their corresponding species.
5. With a decaying driving force across the module length, the difference between feed bulk concentration and wall concentration also decays, causing the concentration polarization factor to decrease in magnitude along the flow direction.
6. Employing longer modules to increase module recovery was shown to be less effective at low applied pressures as the driving force decays along the module, making the additional membrane area less effective for permeate recovery.

7. Comparing the marginal increase in recovery ratio to the marginal increase in applied pressure shows that raising the applied pressure could lead to lower specific energy consumption if the recovery ratio grows at a greater rate relative to the applied pressure.

Acknowledgements

This research is supported by the National Research Foundation (NRF) Singapore under its Campus for Research Excellence and Technological Enterprise (CREATE) programme. The Center for Environmental Sensing and Modeling (CENSAM) is an interdisciplinary research group (IRG) of the Singapore MIT Alliance for Research and Technology (SMART) centre. The authors thank: Yagnaseni Roy for advice on NF modeling; Leonardo D. Banchik for sharing his expertise on operation, design, and modeling of membrane cross-flow systems; and Gregory P. Thiel for offering helpful insights on osmotic pressure modeling. Omar Labban acknowledges the financial support received from an MIT Pappalardo fellowship.

Appendix A. Characterization of Nanofiltration Membranes:

The membrane characterization protocol adopted in this study follows that laid out previously in another work [13]. The procedure consists of running four experiments to characterize a membrane's pore size, effective thickness, charge density, and pore dielectric constant. The membrane pore size and effective thickness are characterized by running pure water permeability (PWP) and uncharged solute experiments, while the charge density and pore dielectric constant are characterized with single salt and synthetic seawater experiments. In this section, a brief overview is provided for completeness. For more details, readers are referred to the original work [13] presented previously.

A.1. Characterization of the membrane pore size and effective thickness

The first step in membrane characterization involves defining a pore size and an effective thickness. The method adopted herein is in tandem to that of Bowen et al. [66], who in an earlier work presented an analytical solution for the uncharged solute rejection as a function of pore size and thickness for a specified flux, J_v:

$$R_{i,\text{real}} = 1 - \frac{c_{i,p}}{c_{i,w}} = 1 - \frac{K_{i,c}\Phi_i}{1 - \exp(-\text{Pe}_{i,w})[1 - \Phi_i K_{i,c}]} \tag{43}$$

$$\text{Pe}_{i,w} = \frac{K_{i,c}}{K_{i,d}} \frac{J_v \Delta x_e}{D_{i,\infty}} \tag{44}$$

where $\text{Pe}_{i,w}$ is the Péclet number comparing diffusive and convective transport in the pores, while the other parameters are defined as in Section 2.2.2. The result accounts for concentration polarization by considering the concentration at the membrane wall $c_{i,w}$. At very high fluxes, this result approaches a simpler form, termed the limiting rejection [66]:

$$R_{i,\text{lim}} = 1 - K_{i,c}\Phi_i \tag{45}$$

Employing Eqs. 43 - 45 to estimate an effective membrane pore size and thickness requires the measurement of the real rejection for uncharged solutes. Accordingly, experiments are set up such that the observed and real rejections are close by limiting concentration polarization. To that end, uncharged solute experiments in this work were operated under low concentrations (200 mg/kg), low applied pressures (1 - 4 bar), and large cross-flow velocities (0.3 m/s). With these experiments, an effective pore size and thickness are then defined for each solute using Eqs. 43 - 44 by regression [13].

Under the assumption that uncharged solute rejection is unaffected by Donnan and dielectric effects, *Nanofiltran* was run at exceedingly large fluxes using the parameters fitted to estimate each solute's limiting rejection (while setting $X_d = 0$ and $\varepsilon_p = \varepsilon_b = 80.4$). The results were then used to fit for a membrane effective pore size with the help of Eq. 45 for later use in all subsequent analyses. Once the pore size was defined, the membrane effective thickness was then estimated from PWP experiments using the Hagen-Poiseuille equation (given by Eq. 3).

A.2. Characterization of the membrane pore dielectric constant and charge density

With the effective pore size and thickness defined, the following step in membrane characterization involves defining the membrane's dielectric constant, ε_p. While varying pH, single salt experiments (e.g. NaCl) are conducted to locate the membrane's isoelectric point, where salt rejection is minimized, the membrane is assumed to be neutrally charged and the pore dielectric constant may be fitted by regression.

The final step in membrane characterization is determining the membrane's charge density, whose estimates are feed-specific, varying with feed pH and composition. For this reason, experiments are conducted with the feed composition of interest to the work, such as the synthetic seawater provided in Table 2. Similar to the pore dielectric constant, regression is then used in estimating the membrane charge. Once this step is completed, validation against experimental results is necessary to ensure the parameters obtained truly represent the membrane under consideration.

A.3. Experimental results employed in membrane characterization

In this section of the Appendix, the experimental results obtained and used for the characterization of the LbL1.5C are provided for completeness. These results have been adapted from an earlier work [13], to which the reader is referred for more details. For all experiments, the cross-flow velocity was maintained at 0.3 m/s to mitigate the effect of concentration polarization. For the uncharged solute and single salt experiments, the flux values recorded were close to those reported for the PWP in light of the low concentrations considered.

Table 5: LbL1.5C pure water permeability (PWP) measurements.

Pressure applied	1 bar	2 bar	3 bar	4 bar
Flux (L/m^2·h)	10	20	30	40

Table 6: LbL1.5C uncharged solute experimental results for a concentration of 200 mg/kg.

Pressure Applied	1 bar	2 bar	3 bar	4 bar
Glycerol Rejection (%)	11	15	20	29
Glucose Rejection (%)	74	77	83	83
Sucrose Rejection (%)	93	94	93	92

Table 7: LbL1.5C single salt experimental rejection (1000 mg/kg NaCl).

	NaCl rejection (%)			
Feed pH	1 bar	2 bar	3 bar	4 bar
5	20	31	35	36
6	17	28	31	33
7	14	20	24	25
8	14	17	18	18
9	18	22	32	34

Table 8: LbL1.5C seawater experimental rejection (composition as per Table 2).

	Synthetic seawater ion rejection (%)					
Applied Pressure	Na^{+}	Ca^{+2}	Mg^{+2}	SO_4^{2-}	Cl^{-}	Flux (LMH)
2 bar	−1.4	54.5	83.4	82.7	11	1.4
3 bar	−0.6	71.1	90.6	85.4	13	3.9
4 bar	1.17	78.9	93.6	86.8	15	6.0

References

[1] P. Eriksson, Nanofiltration extends the range of membrane filtration, Environmental Progress 7 (1) (1988) 58–62. doi:10.1002/ep.3300070116.
URL http://dx.doi.org/10.1002/ep.3300070116

[2] A. Mohammad, Y. Teow, W. Ang, Y. Chung, D. Oatley-Radcliffe, N. Hilal, Nanofiltration membranes review: Recent advances and future prospects, Desalination 356 (2015) 226 – 254, State-of-the-Art Reviews in Desalination. doi:10.1016/j.desal.2014.10.043.
URL http://www.sciencedirect.com/science/article/pii/S0011916414005773

[3] C. Liu, L. Shi, R. Wang, Enhanced hollow fiber membrane performance via semi-dynamic layer-by-layer polyelectrolyte inner surface deposition for nanofiltration and forward osmosis applications, Reactive and Functional Polymers 86 (2015) 154 – 160. doi:10.1016/j.reactfunctpolym.2014.07.018.
URL http://www.sciencedirect.com/science/article/pii/S138151481400145X

[4] C. Liu, L. Shi, R. Wang, Crosslinked layer-by-layer polyelectrolyte nanofiltration hollow fiber membrane for low-pressure water softening with the presence of SO_4^{2-} in feed water, Journal of Membrane Science 486 (2015) 169 – 176. doi:10.1016/j.memsci.2015.03.050.
URL http://www.sciencedirect.com/science/article/pii/S0376738815002380

[5] O. Labban, C. Liu, T. H. Chong, J. H. Lienhard, Relating transport modeling to nanofiltration membrane fabrication: Navigating the permeability-selectivity trade-off in desalination pretreatment, Journal of Membrane Science 554 (2018) 26 – 38. doi:10.1016/j.memsci.2018.02.053.
URL http://www.sciencedirect.com/science/article/pii/S0376738817331617

[6] H. Sombekke, D. Voorhoeve, P. Hiemstra, Environmental impact assessment of groundwater treatment with nanofiltration, Desalination 113 (2–3) (1997) 293 – 296, Workshop on Membranes in Drinking Water Production Technical Innovations and Health Aspects. doi:10.1016/S0011-9164(97)00144-6.
URL http://www.sciencedirect.com/science/article/pii/S0011916497001446

[7] R. A. Bergman, Membrane softening versus lime softening in Florida: A cost comparison update, Desalination 102 (1–3) (1995) 11 – 24, Proceedings of the American Desalting Association 1994 Biennial Conference and Exposition Membrane and Desalting Technologies. doi:10.1016/0011-9164(95)00036-2.
URL http://www.sciencedirect.com/science/article/pii/0011916495000362

[8] W. L. Ang, A. W. Mohammad, N. Hilal, C. P. Leo, A review on the applicability of integrated/hybrid membrane processes in water treatment and desalination plants, Desalination 363 (2015) 2 – 18, hybrid Systems for Desalination. doi:10.1016/j.desal.2014.03.008.
URL http://www.sciencedirect.com/science/article/pii/S0011916414001337

[9] M. Park, J. Park, E. Lee, J. Khim, J. Cho, Application of nanofiltration pretreatment to remove divalent ions for economical seawater reverse osmosis desalination, Desalination and Water Treatment (2015) 1–10arXiv:http://dx.doi.org/10.1080/19443994.2015.1111807, doi:10.1080/19443994.2015.1111807.
URL http://dx.doi.org/10.1080/19443994.2015.1111807

[10] Y. Roy, G. P. Thiel, M. A. Antar, J. H. Lienhard V, The effect of increased top brine temperature on the performance and design of OT-MSF using a case study, Desalination 412 (2017) 32 – 38. doi:10.1016/j.desal.2017.02.015.
URL http://www.sciencedirect.com/science/article/pii/S0011916416320422

[11] Y. Roy, D. M. Warsinger, J. H. Lienhard V, Effect of temperature on ion transport in nanofiltration membranes: Diffusion, convection and electromigration, Desalination 420 (2017) 241 – 257. doi:10.1016/j.desal.2017.07.020.
URL http://www.sciencedirect.com/science/article/pii/S0011916417304745

[12] V. Geraldes, A. M. B. Alves, Computer program for simulation of mass transport in nanofiltration membranes, Journal of Membrane Science 321 (2) (2008) 172 – 182. doi:10.1016/j.memsci.2008.04.054.
URL http://www.sciencedirect.com/science/article/pii/S037673880800392X

[13] O. Labban, C. Liu, T. H. Chong, J. H. Lienhard V, Fundamentals of low-pressure nanofiltration: Membrane characterization, modeling, and understanding the multi-ionic interactions in water softening, Journal of Membrane Science 521 (2017) 18 – 32. doi:http://dx.doi.org/10.1016/j.memsci.2016.08.062.
URL http://www.sciencedirect.com/science/article/pii/S0376738816307050

[14] H. I. Mahon, Permeability separatory apparatus, permeability separatory membrane element, method of making the same and process utilizing the same, U.S. Patent No. 3,228,876 (Jan. 11 1966).

[15] R. R. Donald, M. W. Everett, M. J. Murdock, Fluid separation process and apparatus, U.S. Patent No. 3,339,341 (Sep. 5 1967).

[16] R. W. Baker, Membrane Technology and Applications, John Wiley & Sons, Ltd, 2004. doi:10.1002/0470020393.
URL http://dx.doi.org/10.1002/0470020393

[17] C. Feng, K. Khulbe, T. Matsuura, A. Ismail, Recent progresses in polymeric hollow fiber membrane preparation, characterization and applications, Separation and Purification Technology 111 (2013) 43 – 71. doi:10.1016/j.seppur.2013.03.017.
URL http://www.sciencedirect.com/science/article/pii/S138358661300155X

[18] J. Hermans, Hydrodynamics of hollow fiber reverse osmosis modules, Membrane Digest 1.3 (1972).

[19] W. N. Gill, B. Bansal, Hollow fiber reverse osmosis systems analysis and design, AIChE Journal 19 (4) (1973) 823–831. doi:10.1002/aic.690190422.
URL http://dx.doi.org/10.1002/aic.690190422

[20] M. S. Dandavati, M. R. Doshi, W. N. Gill, Hollow fiber reverse osmosis: experiments and analysis of radial flow systems, Chemical Engineering Science 30 (8) (1975) 877 – 886. doi:10.1016/0009-2509(75)80052-2.
URL http://www.sciencedirect.com/science/article/pii/0009250975800522

[21] H. Ohya, H. Nakajima, K. Takagi, S. Kagawa, Y. Negishi, An analysis of reverse osmotic characteristics of B-9 hollow fiber module, Desalination 21 (3) (1977) 257 – 274. doi:10.1016/S0011-9164(00)88245-4.
URL http://www.sciencedirect.com/science/article/pii/S0011916400882454

[22] N. C. Mat, Y. Lou, G. G. Lipscomb, Hollow fiber membrane modules, Current Opinion in Chemical Engineering 4 (2014) 18 – 24. doi:10.1016/j.coche.2014.01.002.
URL http://www.sciencedirect.com/science/article/pii/S2211339814000033

[23] S. Wickramasinghe, M. J. Semmens, E. Cussler, Mass transfer in various hollow fiber geometries, Journal of Membrane Science 69 (3) (1992) 235 – 250. doi:10.1016/0376-7388(92)80042-I.
URL http://www.sciencedirect.com/science/article/pii/037673889280042I

[24] S. Elmore, G. G. Lipscomb, Analytical approximations of the effect of a fiber size distribution on the performance of hollow fiber membrane separation devices, Journal of Membrane Science 98 (1–2) (1995) 49 – 56. doi:10.1016/0376-7388(94)00174-W.
URL http://www.sciencedirect.com/science/article/pii/037673889400174W

[25] V. Chen, M. Hlavacek, Application of Voronoi tessellation for modeling randomly packed hollow-fiber bundles, AIChE Journal 40 (4) (1994) 606–612. doi:10.1002/aic.690400405.
URL http://dx.doi.org/10.1002/aic.690400405

[26] L.-Z. Zhang, Heat and mass transfer in a randomly packed hollow fiber membrane module: A fractal model approach, International Journal of Heat and Mass Transfer 54 (13–14) (2011) 2921 – 2931. doi:10.1016/j.ijheatmasstransfer.2011.03.005.
URL http://www.sciencedirect.com/science/article/pii/S0017931011001244

[27] D. L. Oatley-Radcliffe, S. R. Williams, M. S. Barrow, P. M. Williams, Critical appraisal of current nanofiltration modelling strategies for seawater desalination and further insights on dielectric exclusion, Desalination 343 (2014) 154 – 161. doi:10.1016/j.desal.2013.10.001.
URL http://www.sciencedirect.com/science/article/pii/S001191641300461X

[28] T. Tsuru, S. Nakao, S. Kimura, Calculation of ion rejection by extended Nernst–Planck equation with charged reverse osmosis membranes for single and mixed electrolyte solutions, Journal of Chemical Engineering of Japan 24 (4) (1991) 511–517. doi:10.1252/jcej.24.511.

[29] Y. Roy, M. H. Sharqawy, J. H. Lienhard V, Modeling of flat-sheet and spiral-wound nanofiltration configurations and its application in seawater nanofiltration, Journal of Membrane Science 493 (2015) 360 – 372. doi:10.1016/j.memsci.2015.06.030.
URL http://www.sciencedirect.com/science/article/pii/S0376738815300028

[30] M. H. Sharqawy, J. H. Lienhard V, S. M. Zubair, Thermophysical properties of seawater: a review of existing correlations and data, Desalination and Water Treatment 16 (1-3) (2010) 354–380. arXiv:http://dx.doi.org/10.5004/dwt.2010.1079, doi:10.5004/dwt.2010.1079.
URL http://dx.doi.org/10.5004/dwt.2010.1079

[31] K. G. Nayar, M. H. Sharqawy, L. D. Banchik, J. H. Lienhard V, Thermophysical properties of seawater: A review and new correlations that include pressure dependence, Desalination 390 (2016) 1 – 24. doi:10.1016/j.desal.2016.02.024.
URL http://www.sciencedirect.com/science/article/pii/S0011916416300807

[32] W. Bowen, A. Wahab Mohammad, Diafiltration by nanofiltration: Prediction and optimization, AIChE Journal 44 (8) (1998) 1799–1812. doi:10.1002/aic.690440811.
URL http://dx.doi.org/10.1002/aic.690440811

[33] W. Bowen, J. S. Welfoot, Modelling the performance of membrane nanofiltration—critical assessment and model development, Chemical Engineering Science 57 (7) (2002) 1121 – 1137. doi:10.1016/S0009-2509(01)00413-4.
URL http://www.sciencedirect.com/science/article/pii/S0009250901004134

[34] W. Bowen, A. Mohammad, Characterization and prediction of nanofiltration membrane performance—a general assessment, Chemical Engineering Research and Design 76 (8) (1998) 885 – 893, separation Processes. doi:10.1205/026387698525685.
URL http://www.sciencedirect.com/science/article/pii/S0263876298717253

[35] G. H. McKinley, 2.25, Advanced Fluid Mechanics, Fall 2013. Massachusetts Institute of Technology: MIT OpenCourseWare, http://ocw.mit.edu, (Accessed 11 Apr 2016).
URL http://ocw.mit.edu

[36] F. M. White, Fluid Mechanics, Seventh Edition, McGraw-Hill Education, 2010.

[37] F. Lipnizki, R. W. Field, Mass transfer performance for hollow fibre modules with shell-side axial feed flow: using an engineering approach to develop a framework, Journal of Membrane Science 193 (2)

(2001) 195 – 208. doi:10.1016/S0376-7388(01)00512-9.
URL http://www.sciencedirect.com/science/article/pii/S0376738801005129

[38] L. D. Banchik, M. H. Sharqawy, J. H. Lienhard, Effectiveness-mass transfer units (ε-MTU) model of a reverse osmosis membrane mass exchanger, Journal of Membrane Science 458 (2014) 189 – 198. doi:10.1016/j.memsci.2014.01.039.
URL http://www.sciencedirect.com/science/article/pii/S0376738814000520

[39] J. H. Lienhard V, K. H. Mistry, M. H. Sharqawy, G. P. Thiel, Thermodynamics, Exergy, and Energy Efficiency in Desalination Systems, in: H. A. Arafat (Ed.), Desalination Sustainability: A Technical, Socioeconomic, and Environmental Approach, Chpt. 4, Elsevier Publishing Co., 2017.

[40] A. D. Shah, C.-H. Huang, J.-H. Kim, Mechanisms of antibiotic removal by nanofiltration membranes: Model development and application, Journal of Membrane Science 389 (2012) 234 – 244. doi:10.1016/j.memsci.2011.10.034.
URL http://www.sciencedirect.com/science/article/pii/S0376738811007940

[41] S. Déon, A. Escoda, P. Fievet, P. Dutournié, P. Bourseau, How to use a multi-ionic transport model to fully predict rejection of mineral salts by nanofiltration membranes, Chemical Engineering Journal 189-190 (2012) 24 – 31. doi:10.1016/j.cej.2012.02.014.
URL http://www.sciencedirect.com/science/article/pii/S1385894712002094

[42] R. Epsztein, E. Shaulsky, N. Dizge, D. M. Warsinger, M. Elimelech, Role of ionic charge density in donnan exclusion of monovalent anions by nanofiltration, Environmental Science & Technologydoi:10.1021/acs.est.7b06400.

[43] W. Bowen, H. Mukhtar, Characterisation and prediction of separation performance of nanofiltration membranes, Journal of Membrane Science 112 (2) (1996) 263 – 274. doi:10.1016/0376-7388(95)00302-9.
URL http://www.sciencedirect.com/science/article/pii/0376738895003029

[44] P. Dechadilok, W. M. Deen, Hindrance factors for diffusion and convection in pores, Industrial & Engineering Chemistry Research 45 (21) (2006) 6953–6959. doi:10.1021/ie051387n.

[45] D. L. Oatley-Radcliffe, S. R. Williams, T. J. Ainscough, C. Lee, D. J. Johnson, P. M. Williams, Experimental determination of the hydrodynamic forces within nanofiltration membranes and evaluation of the current theoretical descriptions, Separation and Purification Technology 149 (2015) 339 – 348. doi:10.1016/j.seppur.2015.05.041.
URL http://www.sciencedirect.com/science/article/pii/S1383586615300253

[46] G. M. Mavrovouniotis, H. Brenner, Hindered sedimentation, diffusion, and dispersion coefficients for brownian spheres in circular cylindrical pores, Journal of Colloid and Interface Science 124 (1) (1988)

269 – 283. doi:10.1016/0021-9797(88)90348-7.
URL http://www.sciencedirect.com/science/article/pii/0021979788903487

[47] J. Ennis, H. Zhang, G. Stevens, J. Perera, P. Scales, S. Carnie, Mobility of protein through a porous membrane, Journal of Membrane Science 119 (1) (1996) 47 – 58. doi:10.1016/0376-7388(96)00112-3.
URL http://www.sciencedirect.com/science/article/pii/0376738896001123

[48] L. R. Glicksman, J. H. Lienhard V, Modeling and Approximation in Heat Transfer, Cambridge University Press, New York, 2016.
URL http://www.cambridge.org/9781107012172

[49] V. Geraldes, M. D. Afonso, Prediction of the concentration polarization in the nanofiltration/reverse osmosis of dilute multi-ionic solutions, Journal of Membrane Science 300 (1–2) (2007) 20 – 27. doi:10.1016/j.memsci.2007.04.025.
URL http://www.sciencedirect.com/science/article/pii/S0376738807002815

[50] F. G. Donnan, Theory of membrane equilibria and membrane potentials in the presence of non-dialysing electrolytes. a contribution to physical-chemical physiology, Journal of Membrane Science 100 (1) (1995) 45–55.

[51] A. Grodzinsky, Field, Forces and Flows in Biological Systems, Garland Science, London and New York, 2011.

[52] D. L. Parkhurst, C. Appelo, User's guide to PHREEQC (Version 2): A computer program for speciation, batch-reaction, one-dimensional transport, and inverse geochemical calculations.

[53] K. H. Mistry, H. A. Hunter, J. H. Lienhard V, Effect of composition and nonideal solution behavior on desalination calculations for mixed electrolyte solutions with comparison to seawater, Desalination 318 (2013) 34 – 47. doi:10.1016/j.desal.2013.03.015.
URL http://www.sciencedirect.com/science/article/pii/S0011916413001409

[54] R. Silbey, R. Alberty, M. Bawendi, Physical Chemistry 4th edn, Wiley, New York, 2004.

[55] D. L. Oatley, L. Llenas, R. Pérez, P. M. Williams, X. Martínez-Lladó, M. Rovira, Review of the dielectric properties of nanofiltration membranes and verification of the single oriented layer approximation, Advances in Colloid and Interface Science 173 (2012) 1 – 11. doi:10.1016/j.cis.2012.02.001.
URL http://www.sciencedirect.com/science/article/pii/S000186861200022X

[56] S. Bandini, D. Vezzani, Nanofiltration modeling: the role of dielectric exclusion in membrane characterization, Chemical Engineering Science 58 (15) (2003) 3303 – 3326. doi:10.1016/S0009-2509(03)00212-4.
URL http://www.sciencedirect.com/science/article/pii/S0009250903002124

[57] A. E. Yaroshchuk, Dielectric exclusion of ions from membranes, Advances in Colloid and Interface Science 85 (2–3) (2000) 193 – 230. doi:10.1016/S0001-8686(99)00021-4.
URL http://www.sciencedirect.com/science/article/pii/S0001868699000214

[58] K. Dill, S. Bromberg, Molecular driving forces: statistical thermodynamics in biology, chemistry, physics, and nanoscience, Garland Science, 2010.

[59] G. K. Pearce, UF/MF Membrane Water Treatment: Principles and Design, Water Treatment Academy Bangkok, 2011.

[60] DOW Chemical Company, Ultrafiltration Product Manual, 2011.

[61] Koch Membrane Systems, Puron MP Hollow Fiber Cartridge, 2015.

[62] W. R. Bowen, J. S. Welfoot, P. M. Williams, Linearized transport model for nanofiltration: Development and assessment, AIChE Journal 48 (4) (2002) 760–773. doi:10.1002/aic.690480411.
URL http://dx.doi.org/10.1002/aic.690480411

[63] T. Tsuru, M. Urairi, S.-I. Nakao, S. Kimura, Negative rejection of anions in the loose reverse osmosis separation of mono-and divalent ion mixtures, Desalination 81 (1-3) (1991) 219–227.

[64] A. E. Yaroshchuk, Negative rejection of ions in pressure-driven membrane processes, Advances in Colloid and Interface Science 139 (1–2) (2008) 150 – 173, membrane Electrochemistry: Selected papers from the 33rd Conference on Membrane Electrochemistry, Russia, May 2007. doi:10.1016/j.cis.2008.01.004.
URL http://www.sciencedirect.com/science/article/pii/S0001868608000328

[65] M. Costello, A. Fane, P. Hogan, R. Schofield, The effect of shell side hydrodynamics on the performance of axial flow hollow fibre modules, Journal of Membrane Science 80 (1) (1993) 1 – 11. doi:10.1016/0376-7388(93)85127-I.
URL http://www.sciencedirect.com/science/article/pii/037673889385127I

[66] W. Bowen, A. Mohammad, N. Hilal, Characterisation of nanofiltration membranes for predictive purposes — use of salts, uncharged solutes and atomic force microscopy, Journal of Membrane Science 126 (1) (1997) 91 – 105. doi:10.1016/S0376-7388(96)00276-1.
URL http://www.sciencedirect.com/science/article/pii/S0376738896002761